Supplement of The Cryosphere, 19, 5045–5073, 2025 https://doi.org/10.5194/tc-19-5045-2025-supplement © Author(s) 2025. CC BY 4.0 License.





Supplement of

Comprehensive assessment of stress calculations for crevasse depths and testing with crevasse penetration as damage

Benjamin Reynolds et al.

Correspondence to: Benjamin Reynolds (breynold@caltech.edu)

The copyright of individual parts of the supplement might differ from the article licence.

S1: Strain Rates Maps

10

Strain rates are calculated with central differences, the default method in the gradient function of both MATLAB and NumPy. No smoothing was applied.

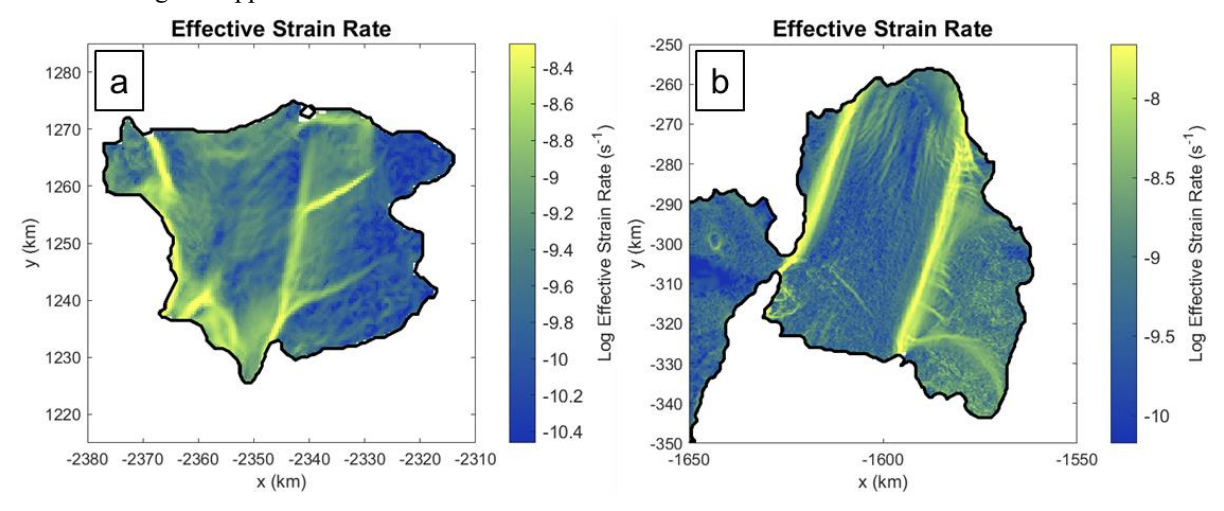


Figure S1: Log effective strain rate plots of (a) the Scar Inlet ice shelf and (b) the Pine Island Glacier Ice Shelf.

S2: Brunt/Stancomb-Wills Ice Shelf Cross Sections

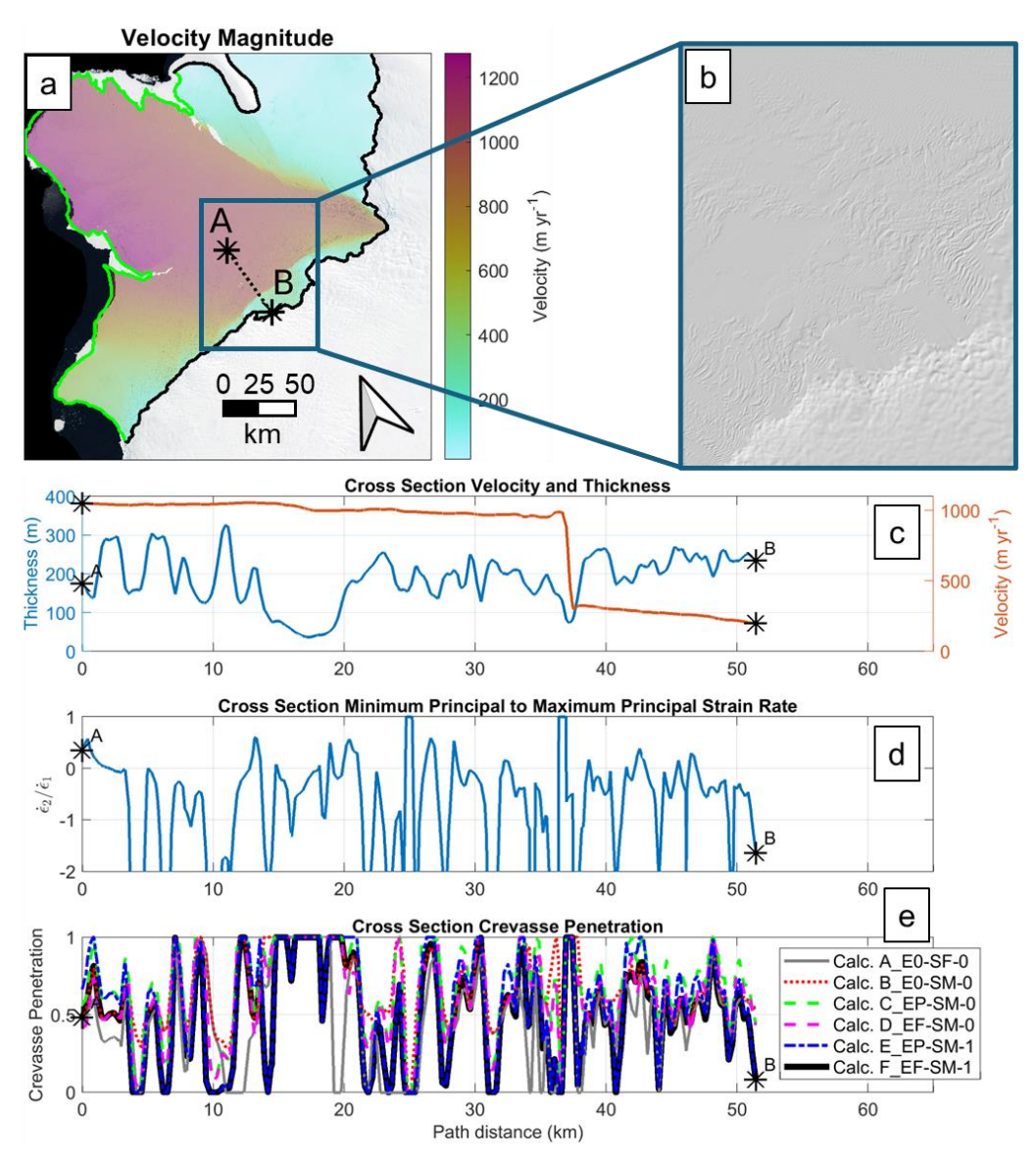


Figure S2: (a) observed velocity (ITS_LIVE 2015 – Rignot et al., 2022) map with cross section location, (b) 2015 hillshade REMA (Howat et al., 2019) snapshot of the southern rift, (c) cross section velocity and thickness, (d) cross section minimum to maximum principal strain rate ratio, and (e) cross section crevasse penetration for the Brunt/Stancomb-Wills ice shelf.

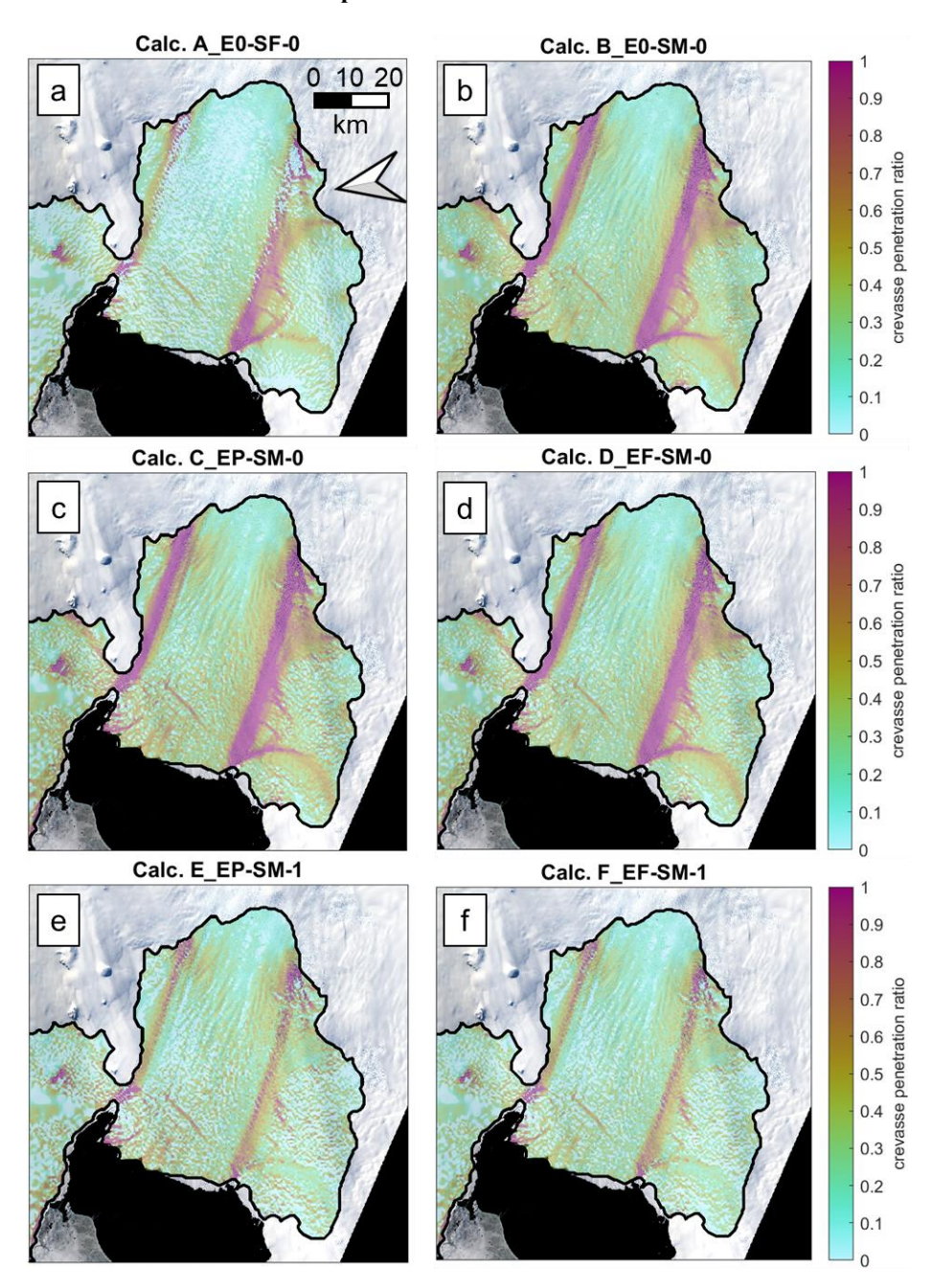


Figure S3: Crevasse penetration at the Pine Island Glacier ice shelf with (a) calculation A_E0-SF-0, (b) calculation B_E0-SM-0, (c) calculation C_EP-SM-0, (d) calculation D_EF-SM-0, (e) calculation E_EP-SM-1, and (f) calculation F_EF-SM-1 resistive stress versions overlaid on satellite imagery from November 2014 (Landsat-8 image courtesy of the U.S. Geological Survey). Ice flow direction is approximately from image top to bottom.

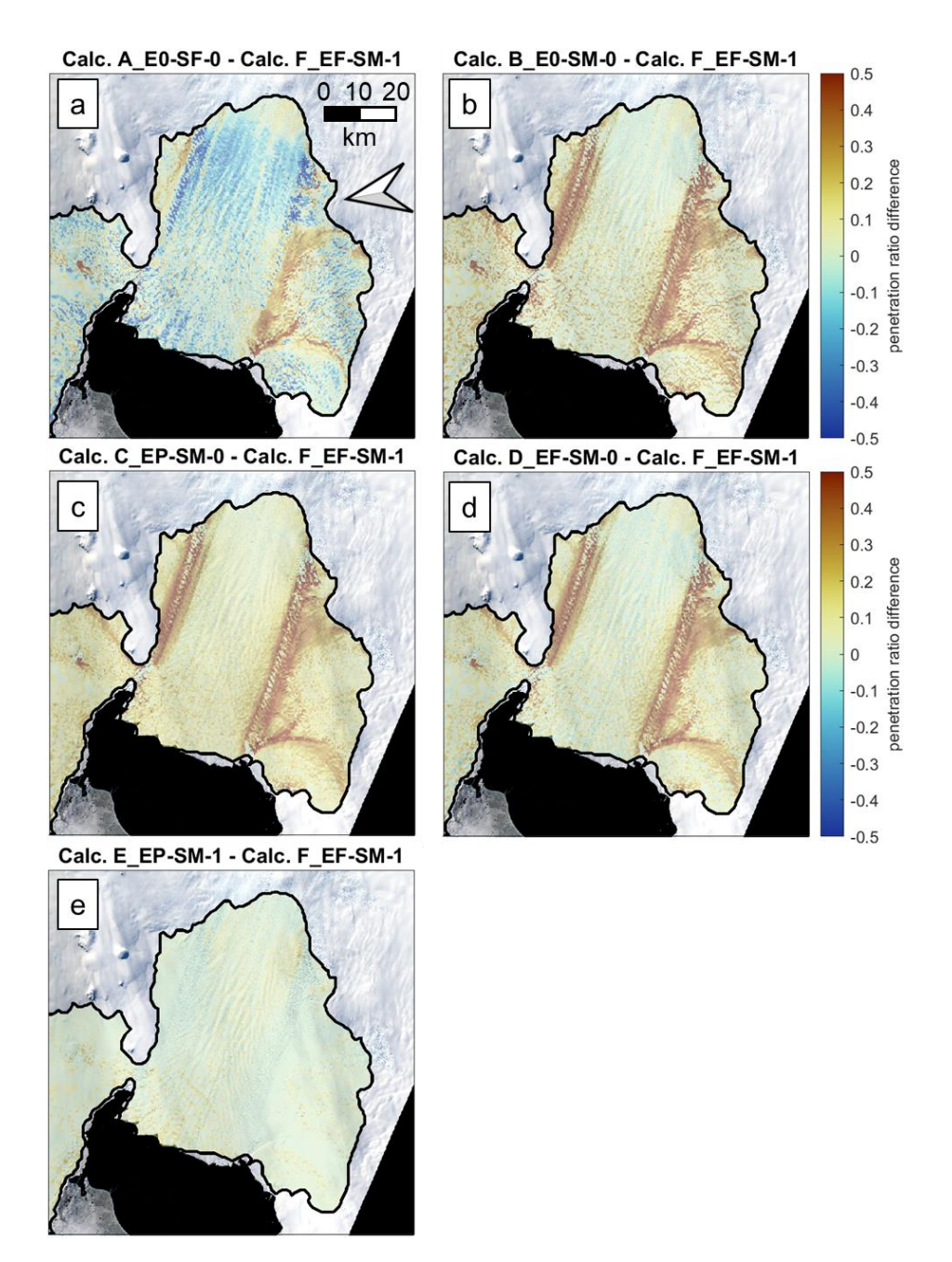
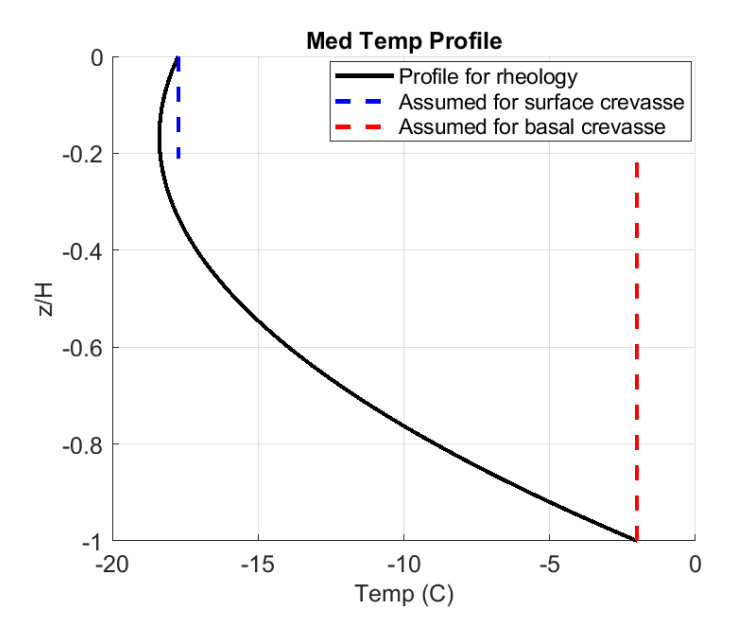


Figure S4: Difference from calculation F_EF-SM-1 crevasse penetration for (a) calculation A_E0-SF-0, (b) calculation B_E0-SM-0, (c) calculation C_EP-SM-0, (d) calculation D_EF-SM-0, and (e) calculation E_EP-SM-1 crevasse penetration at the Pine Island Glacier ice shelf.

30 S4: Temperature Assumptions for Analysis

Fig. S5 shows the temperature profile used for the "no damage" simulation of the Pine Island Glacier shelf. This profile was created by using the average surface temperature from Comiso (2000) at the surface, assuming 5°C colder at a depth of one third the ice thickness, assuming -2°C at the base, and fitting a second-order polynomial through those points. It is expected to be warmer than actual temperatures based on comparison to the limited number of borehole temperature measurements in ice shelves (Humbert, 2010; Wang et al., 2022). The assumed temperatures for surface and basal crevasses (constant in z) are also shown. The tuned background rigidity used in the analyses with crevasse penetration as damage would correspond to a colder (on average) profile than the warm profile shown in Fig. S5, as the resulting background rigidities were higher.



40 Figure S5: Temperature profile used to calculate the average rigidity for the Scar Inlet ice shelf with assumed temperatures for surface and basal crevasses shown.

S5: Modelled Velocity Maps for the Scar Inlet and Pine Island Glacier ice shelves

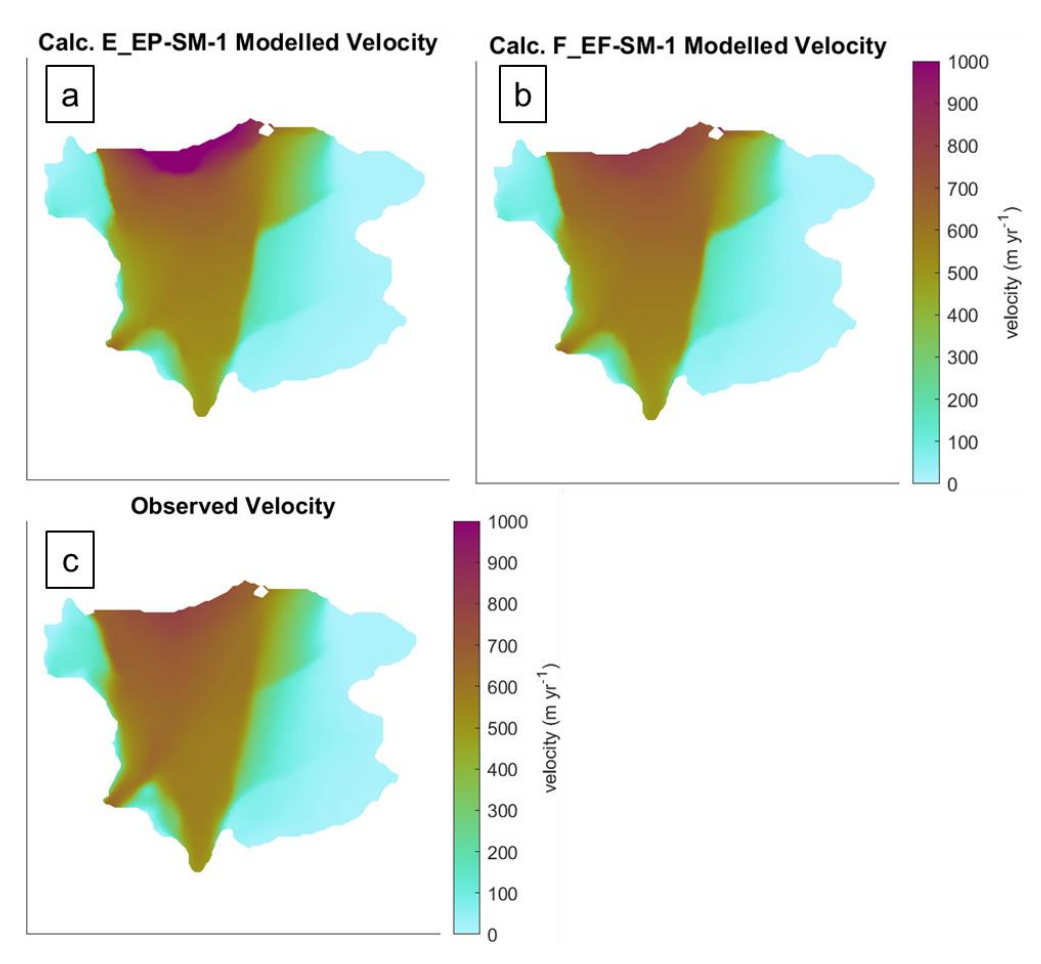


Figure S6: Plots of (a) modelled velocity with calculation E_EP-SM-1, (b) modelled velocity with calculation F_EF-SM-1, and (c) observed velocity for the Larsen B remnant ice shelf. The velocity product used for crevasse penetration calculation and shown in (c) is the MEaSUREs 2014-2017 averaged product (Gardner et al., 2018, 2019).

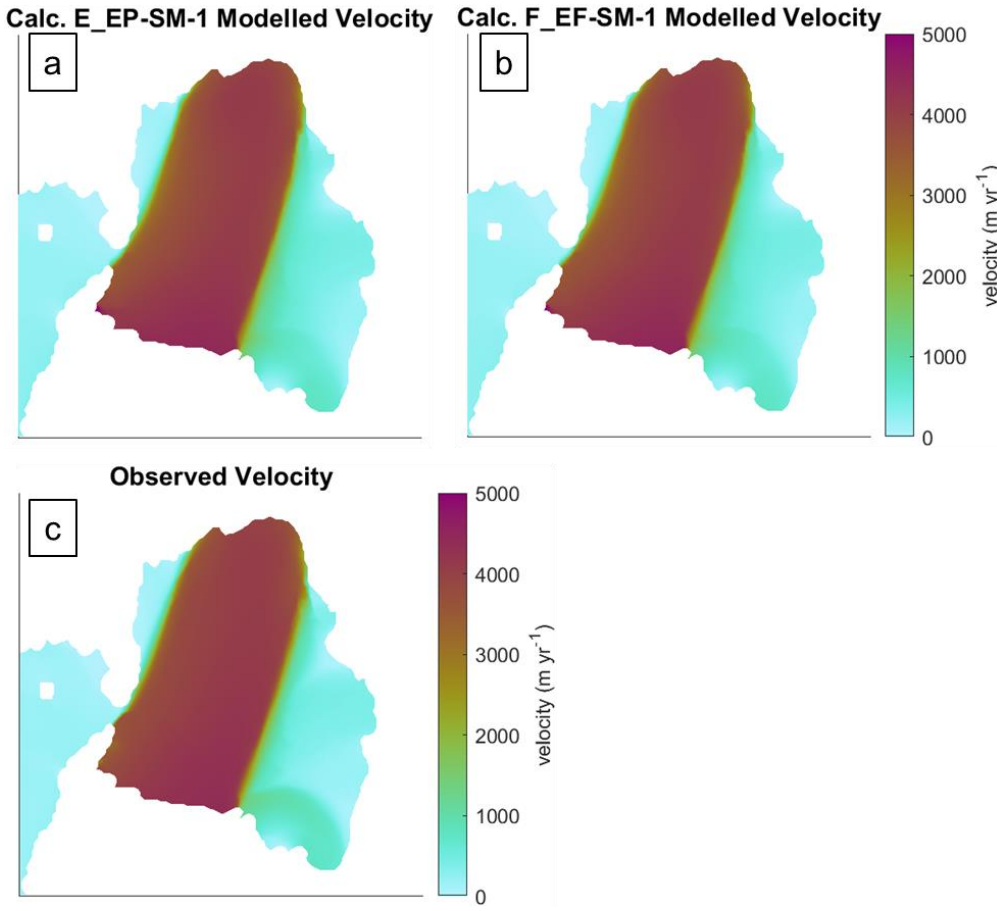


Figure S7: Plots of (a) modelled velocity with calculation E_EP-SM-1, (b) modelled velocity with calculation F_EF-SM-1, and (c) observed velocity for the Pine Island Glacier ice shelf. The velocity product used for crevasse penetration calculation and shown in (c) is the ITS_LIVE 2015 annual map (Rignot et al., 2022).

55 S6: Analysis with n=4 Rheology

Millstein et al. (2022) recently recommended n=4.1 as the best on-average flow exponent by analyzing longitudinal flow regions of several Antarctic ice shelves, which has initiated work assessing the impact of the higher flow exponent (e.g. Getraer and Morlighem, 2025). Millstein et al. (2022) found a range of flow law rate parameters (A) and did not recommend a particular function for determining the parameter from temperature. Experimental work has shown n=4 rheology for relatively high stress deformation (Goldsby and Kohlstedt, 2001) with a transition from n=1.8 at lower stresses that occurs at a grain-size and temperature-dependant stress threshold. We started out using the flow law rate parameter equation and coefficients for n=4 from Goldsby and Kohlstedt (2001), but found that this rheology would predict higher stresses than the n=3 rheology recommended in Cuffey and Patterson (2010) across the complete range of strain rates present in the Scar Inlet and Pine Island ice shelves (Fig. S8). To capture the expected behavior of n=4 versus n=3 rheology, namely less stress in regions of high strain rate but more stress in regions of low strain rate, we adjusted the prefactor A_0 such that the n=4 stress versus strain rate curve intersects that of n=3 (Cuffey and Patterson, 2010) near the median strain rate from these ice shelves. The flow rate paramater, A, is calculated as

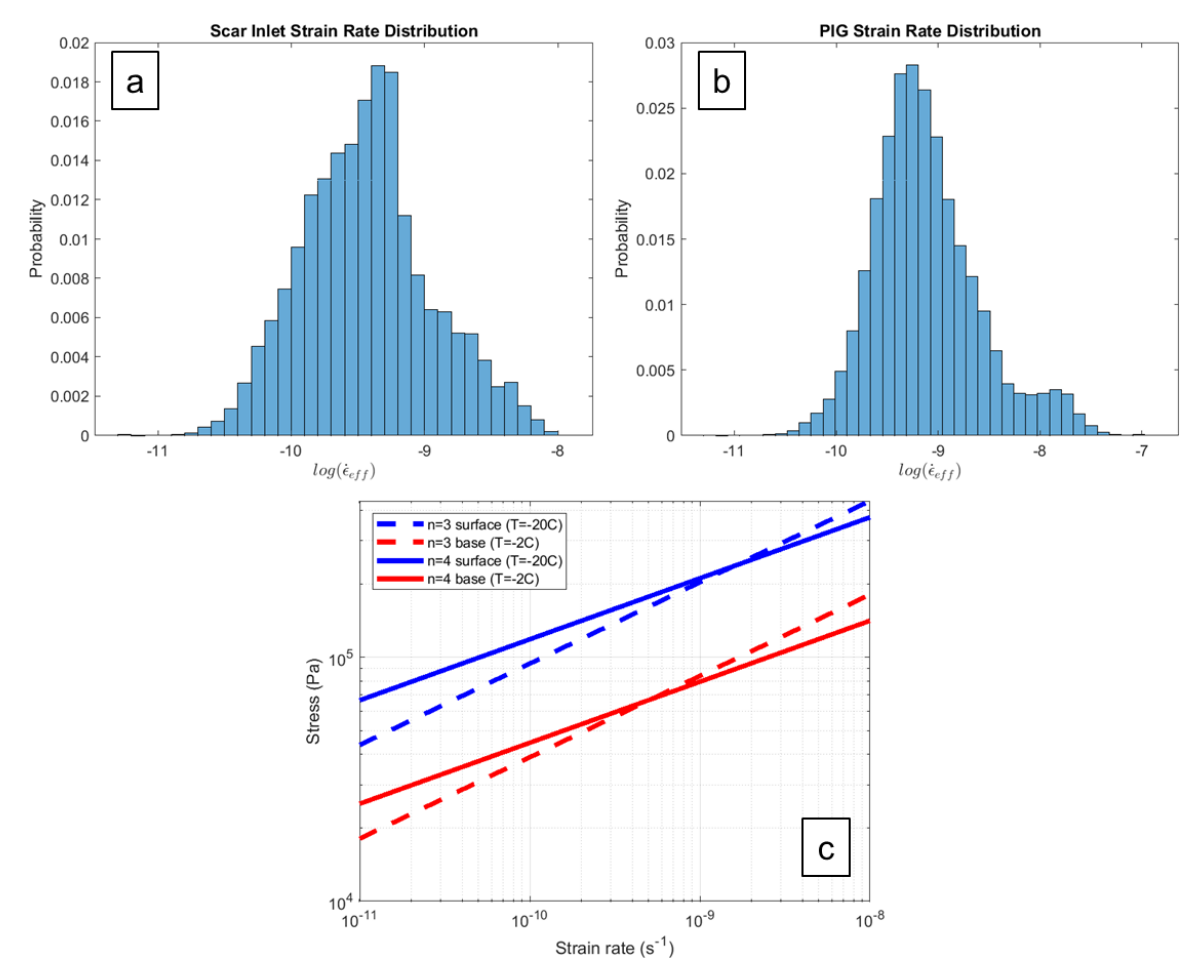
$$A = A_0 exp\left(\frac{-Q_C}{PT}\right) \tag{S1}$$

where A_0 is the prefactor, Q_c is activation energy, R is the ideal gas constant, and T is ice temperature. The values of these parameters we used for warm and cold ice are provide in Table S1. Our threshold temperature, T_* , is 261.17K (-12.00°C) as calculated with

$$T_* = \frac{Q_{c,\text{cold}} - Q_{c,\text{warm}}}{R \ln(A_{0,\text{cold}}/A_{0,\text{warm}})}.$$
 (S2)

Condition	Parameter	Description	Value	Units
<i>T</i> ≤ −12.00°C	A_0	Cold prefactor	6x10 ⁻¹⁹	Pa ⁻⁴ s ⁻¹
	Q_c	Cold activation energy	5.85x10 ⁴	J mol ⁻¹
<i>T</i> > −12.00°C	A_0	Warm prefactor	$1.2x10^6$	Pa ⁻⁴ s ⁻¹
	Q_c	Warm activation energy	1.8x10 ⁵	J mol ⁻¹
n/a	R	Ideal gas constant	8.314	J mol ⁻¹ K ⁻¹

Table S1: Parameter values for calculation of n=4 flow law rate paramater.



80

Figure S8: (a) strain rate distribution of the Scar Inlet ice shelf, (b) strain rate distribution of the Pine Island Glacier ice shelf, and (c) stress versus strain rate at -20°C and -2°C

As guaranteed by our tuning of the prefactor, areas of high strain rate like shear margins see reduction in crevasse penetration, much of the shelf has little change in crevasse penetration, and areas of low strain rate like the slow-moving zones away from glacier inlets see increased crevasse penetration. This pattern of crevasse penetration change from n=3 to n=4 rheology is shown for the Scar Inlet and Pine Island glacier ice shelves in Fig. S9.

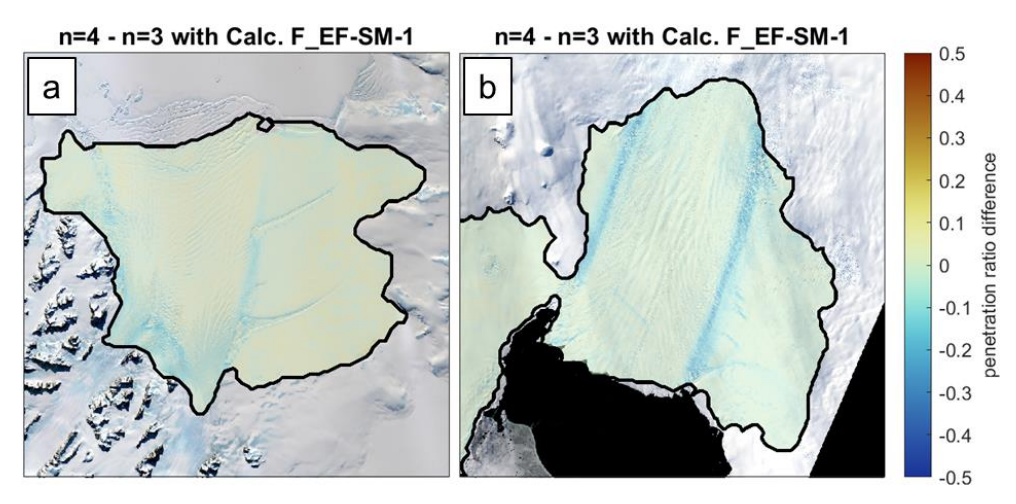


Figure S9: difference in crevasse penetration with n=4 rheology relative to that of n=3 (using stress calculation F_EF-SM-1_ at the (a) Scar Inlet and (b) Pine Island Glacier ice shelves.

With these crevasse penetration fields, we performed the same analysis as performed with crevasse penetration with n=3 rheology and stress calculations $E_EP-SM-1$ and $F_EF-SM-1$ for these two shelves. The goal of this analysis is to assess whether our finding that damage from calculation $F_EF-SM-1$ better reproduces observed velocities is insensitive to the change in flow exponent. The Scar Inlet shelf velocity correlation and misfit maps with these calculations using n=4 (Figure S10) show the same general finding holds: high damage near the front with calculation $E_EP-SM-1$ causes excess velocity that is largely fixed by calculation $F_EF-SM-1$. We tested this analysis with prefactors (A_0) ranging from half to four times greater than those in Table S1 and found that this result still holds. The same figure for the Pine Island Glacier shelf, the modeled velocity fields for Scar Inlet, the modeled velocity fields for Pine Island, and the values of mean absolute velocity misfit are provided as Fig. S11, S12, S13, and S14 respectively.

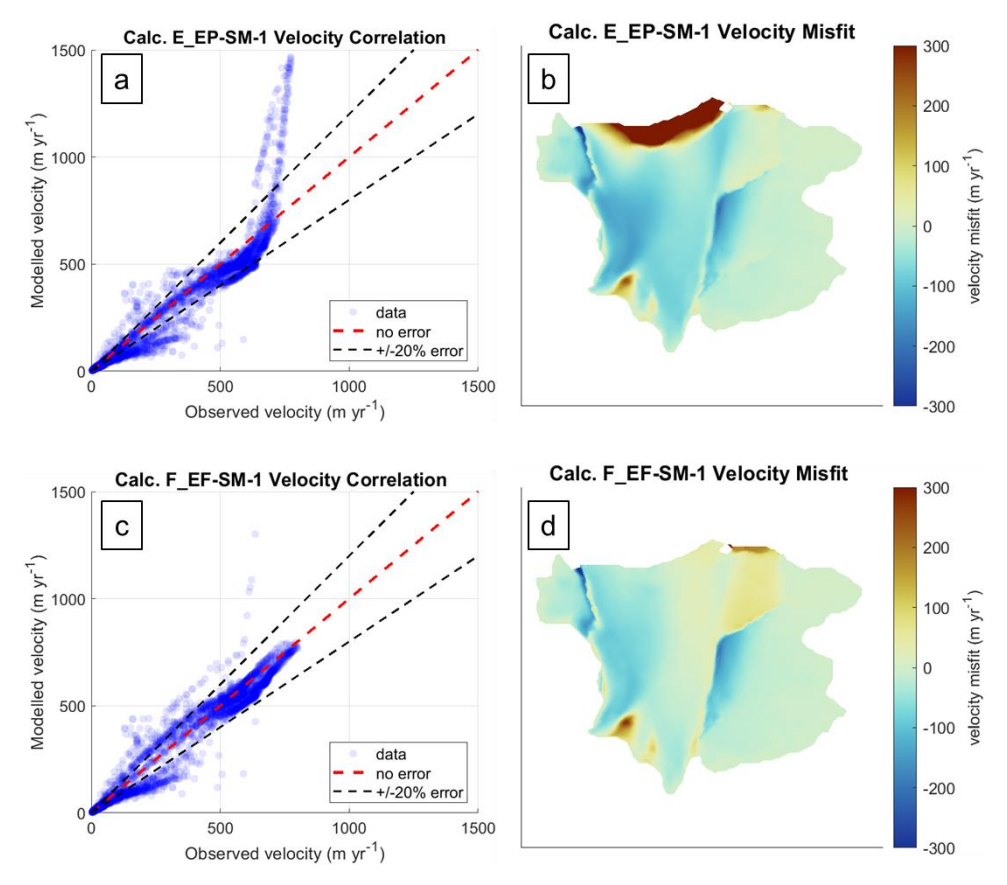


Figure S10: Plots of (a) velocity correlation and (b) velocity misfit with calculation E_EP-SM-1 as well (c) velocity correlation and (d) velocity misfit with calculation F_EF-SM-1 for the Scar Inlet ice shelf with n=4 rheology. The velocity product used for crevasse penetration calculation and correlation plots is the MEaSUREs 2014-2017 averaged product (Gardner et al., 2018, 2019).

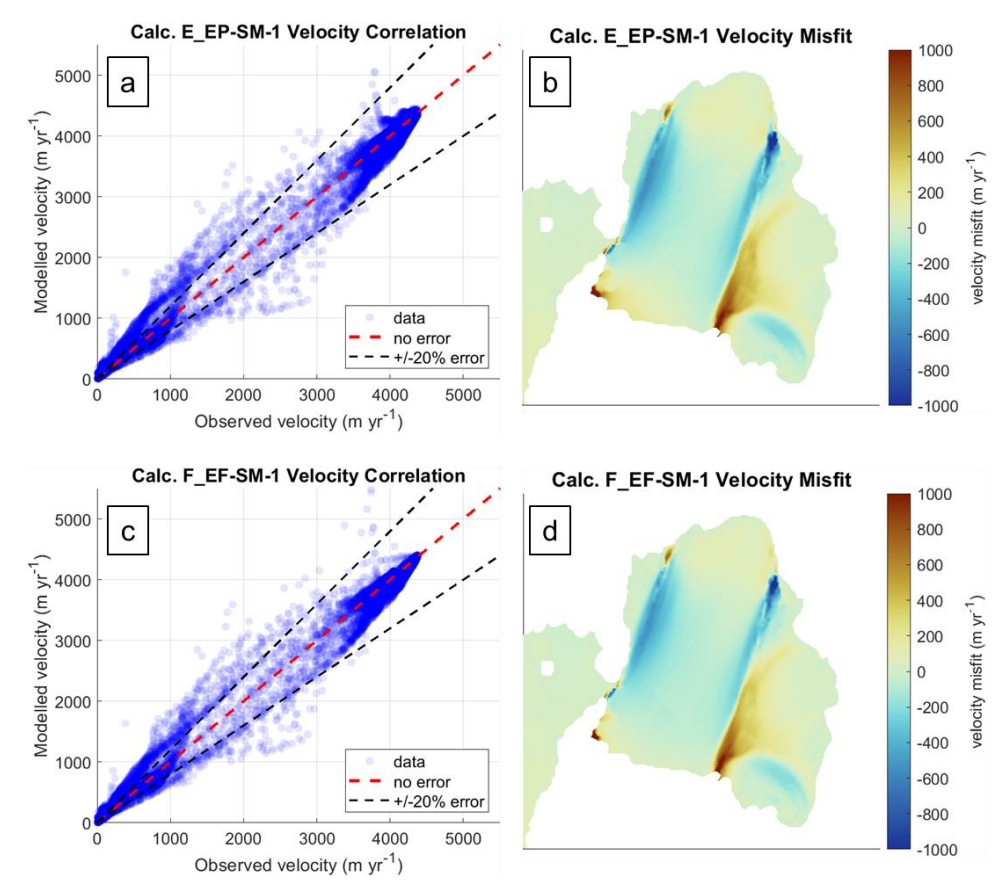


Figure S11: Plots of (a) velocity correlation and (b) velocity misfit with calculation E_EP-SM-1 as well (c) velocity correlation and (d) velocity misfit with calculation F_EF-SM-1 for the Pine Island Glacier ice shelf with n=4 rheology. The velocity product used for crevasse penetration calculation and correlation is the ITS LIVE 2015 annual map (Rignot et al., 2022).

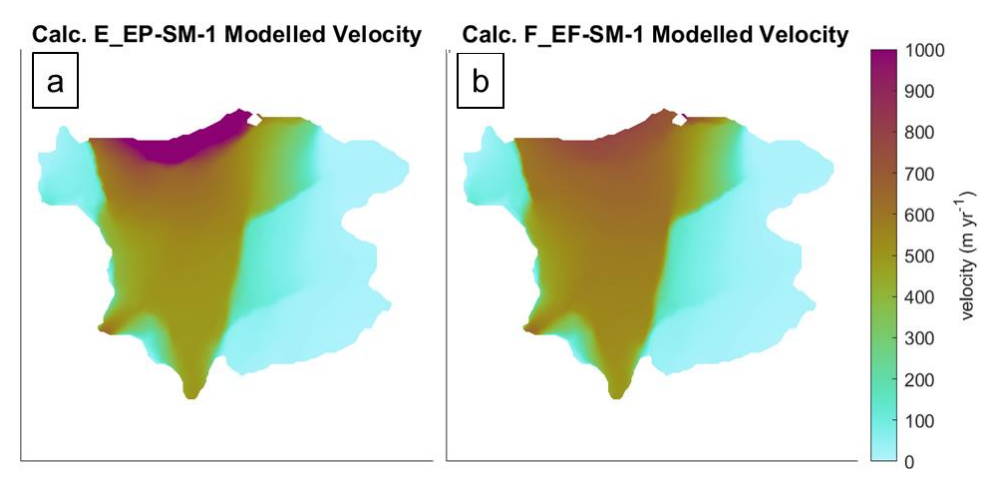


Figure S12: Plots of (a) modelled velocity with calculation E_EP-SM-1 and (b) modelled velocity with calculation F_EF-SM-1 using n=4 rheology for the Scar Inlet ice shelf.

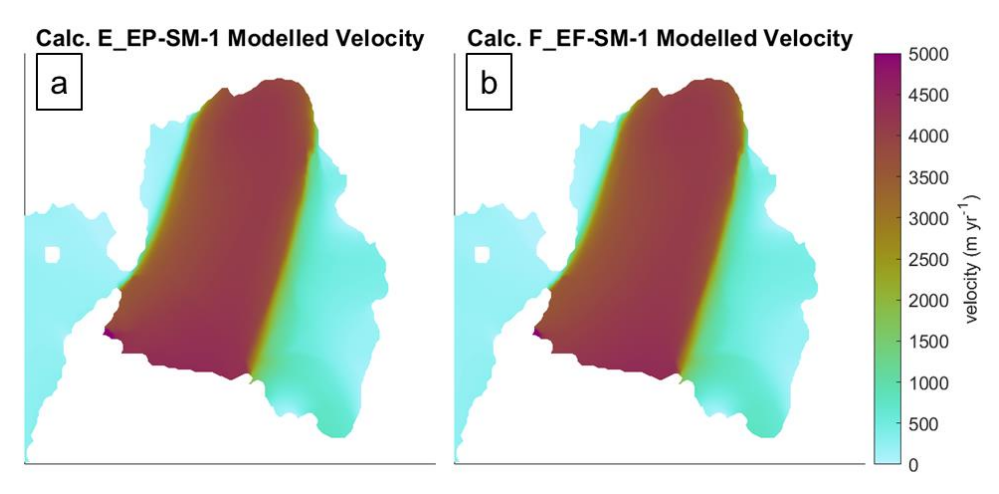
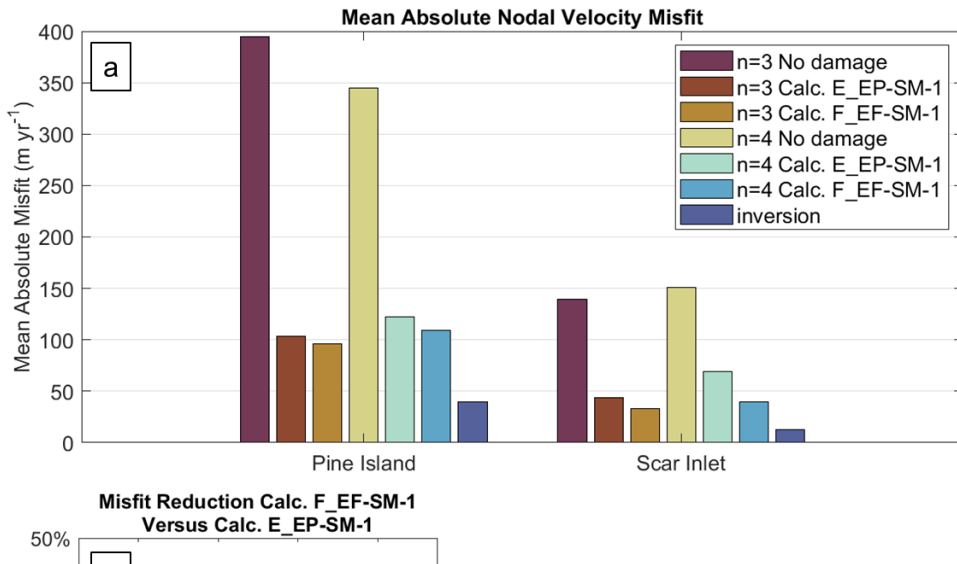


Figure S13: Plots of (a) modelled velocity with calculation E_EP-SM-1 and (b) modelled velocity with calculation F_EF-SM-1 using n=4 rheology for the Pine Island Glacier ice shelf.



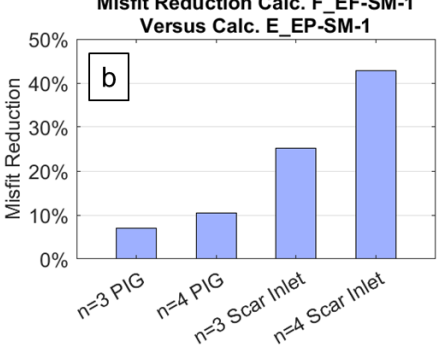


Figure S14: (a) mean absolute velocity misfit for no damage, calculation E_EP-SM-1, and calculation F_EF_SM-1 with n=3 and n=4 rheology as well as for inverted damage and (b) misfit reduction for calculation F_EF-SM-1 relative to E_EP-SM-1 for both shelves with n=3 and n=4 rheology. The n=3 results are identical to those presented in Figure 10 of the main text.

115 S7: Analysis with Longitudinal Force Balance Method

125

130

135

140

145

We also considered the impact of using the force balance method from Buck (2023). We calculated buttressing number, K_n , as in Fürst et al. (2016):

$$K_n = 1 - \frac{R_{XX}}{N_0} \tag{S3}$$

where R_{xx} is the resistive stress and N_0 is the resistive stress corresponding to an ice cliff boundary condition for floating ice

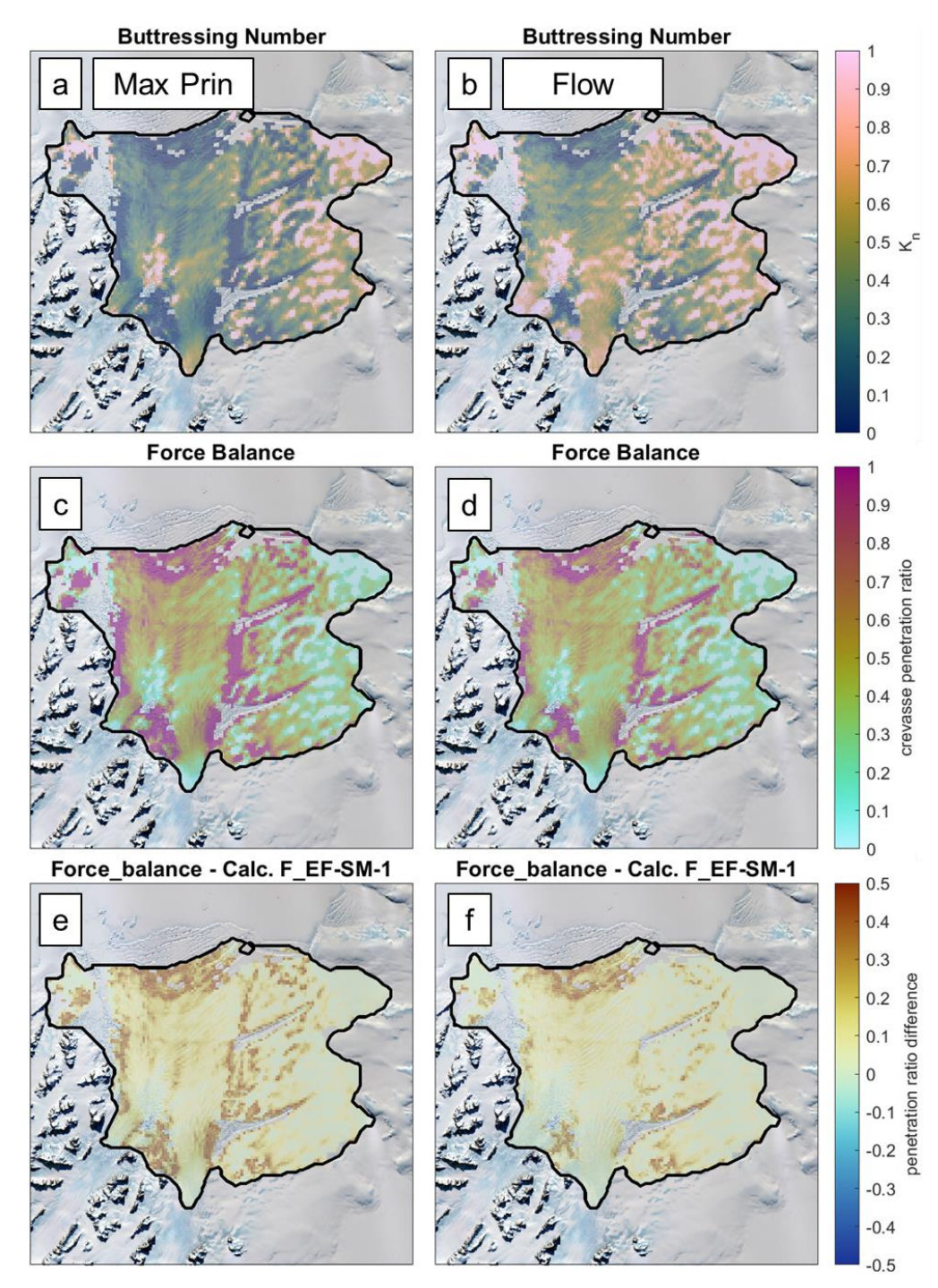
120
$$N_0 = \frac{1}{2} \rho_i g H \left(1 - \frac{\rho_i}{\rho_{nw}} \right)$$
. (S4)

We then use Equations 5 and 6 in the manuscript to determine the ratio of the increased stress to the original resistive stress $R_{xx,1}/R_{xx,0}$, which is the factor by which crevasse sizes will be increased. As we assume crevasses strike perpendicular to the maximum principal stress direction and the force balance method considers water pressure added perpendicular to the crevasse strike, we first used buttressing calculated in the maximum principal stress direction. The resistive stress for this calculation should be the depth-averaged resistive stress, but we used resistive calculated at the assumed base temperature of -2°C, which will tend to reduce the impact of adding force balance. This buttressing number, clipped from zero to one, is shown for the Scar Inlet ice shelf in Fig. S15a. It is zero or near-zero in the shear margins and near the shelf front. This low buttressing number roughly doubles the crevasse penetration in these regions, causing them to go from high but not complete crevasse penetration with the zero stress approximation (with calculation F_EF-SM-1) to complete crevasse penetration. The crevasse penetration and difference between force balance and zero stress approximation crevasse penetration are given as Figure S15 c and e. Because shear margins are not considered in Buck (2023), we repeated the analysis with flow direction buttressing to remove the effect on these regions. The flow direction and maximum principal directions are similar in the center of flow but diverge in shear margins. These results are shown in Fig. S15 b, d, and f. The same results for Pine Island Glacier ice shelf are provided as Fig. S16.

Because of the complete shear margin crevasse penetration predicted for the maximum principal stress direction buttressing number results, we model velocity with crevasse penetration as damage from the flow direction buttressing number result. The velocity correlation and velocity misfit maps for the Scar Inlet and Pine Island Glacier ice shelves are provided in Fig. S17. There is too much speedup at the front of the Scar Inlet shelf, similar to the result of stress calculation E_EP-SM-1 with the zero stress approximation. This results in higher mean absolute velocity misfit for the force balance method at the Scar Inlet shelf (Fig. S18). One possible explanation is that the force balance method applied to stresses calculated from remote-sensing-based strain rates may be partially "double-counting" the self-amplifying effect of crevasses on stress. Namely, a far-field stress exists and initiates crevasses. The basal crevasse adds to the force in the cross section according to the force balance equations in Buck (2023) creating a higher stress carried by the ice ligament. For some area of influence at and around the crevasse, there will be increased strain rate which may increase the spatially averaged remote-sensing velocity measurements. A stress is calculated from this as-measured strain rate and taken to be the far-field resistive stress. The force

balance method is applied assuming this increased stress is the far-field stress if no crevasses were present, so the impact of basal water pressure on crevassing may be applied again leading to some over-accounting of this effect.

For the Pine Island Glacier ice shelf, damage from force balance performs slightly better than damage from the zero stress approximation. Comparing the relevant velocity correlation and velocity misfit plots (Fig. 12c and d for the zero stress approximation and Fig. S17c and d for force balance), there is not as clear of a velocity range or region driving the result. Misfit appears to be more localized in the shear margins particularly in the shear margin of the Southwest Tributary where force balance increased damage relative to the zero stress approximation.



155 Figure S15: (a) buttressing number, (c) crevasse penetration, and (e) difference between force balance crevasse penetration and that of calculation F_EF-SM-1 for buttressing number calculated in the maximum principal stress direction and the same but with buttressing calculated in the flow direction as (b, d, f) for the Scar Inlet ice shelf.

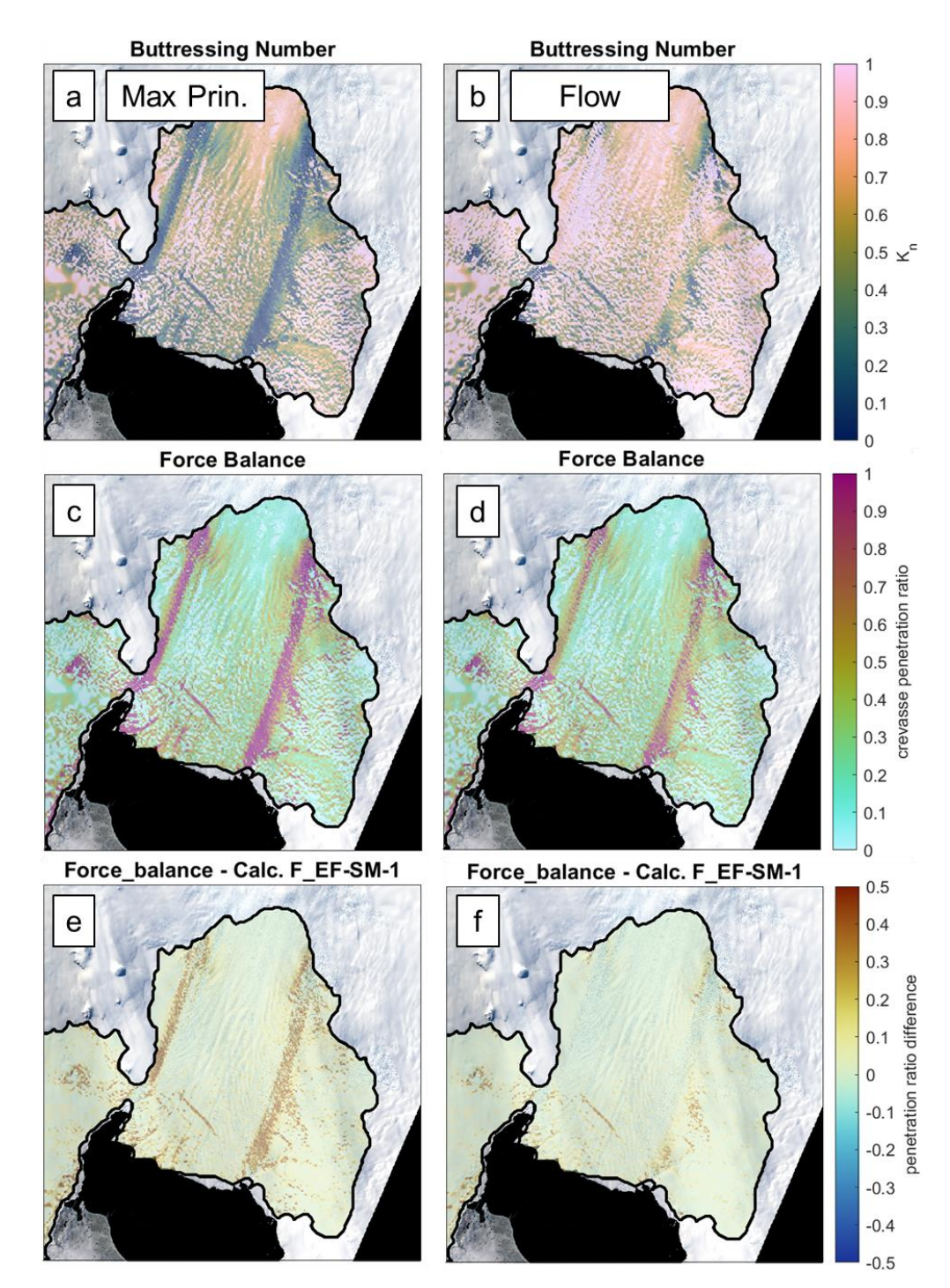


Figure S16: (a) buttressing number, (c) crevasse penetration, and (e) difference between force balance crevasse penetration and that of calculation F_EF-SM-1 for buttressing number calculated in the maximum principal stress direction and the same but with buttressing calculated in the flow direction as (b, d, f) for the Pine Island Glacier ice shelf.

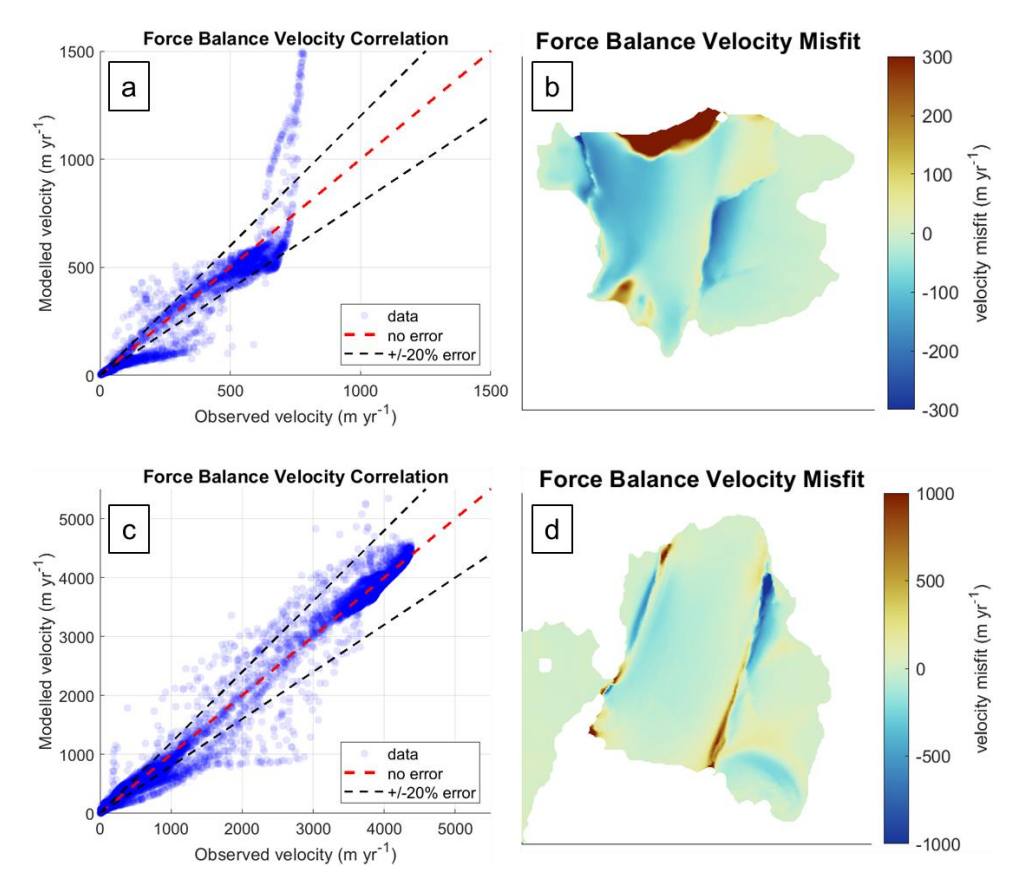


Figure S17: Plots of (a) velocity correlation and (b) velocity misfit with force balance crevasse penetration as damage at Scar Inlet ice shelf and the same at Pine Island Glacier ice shelf (c, d).

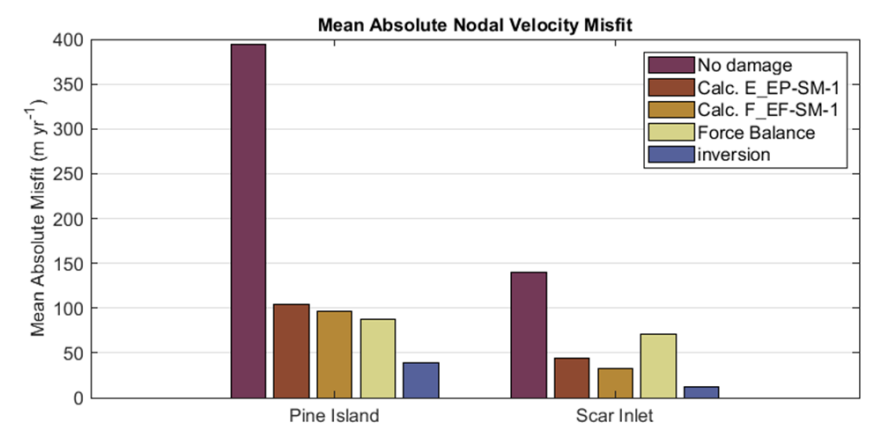


Figure S18: Mean absolute velocity misfit with no damage, zero stress approximation with calculation E_EP-SM-1, zero stress approximation with calculation F_EF-SM-1, force balance (starting with calculation F_EF-SM-1 stress), and inversion. All results except that of force balance are identical to those in Figure 10 in the main text.

S8: Firn density considerations

We did not take firn density into consideration in the surface crevasse depth calculations. Because the surface topography included with BedMachine is corrected for firn density, the amount of ice in terms of integrated density that the crevasse extends through will be the same. (This is true because we used the zero stress approximation. The geometry driven changes in stress intensity factor included in LEFM would mean that the integrated density of ice above the crevasse tip would change.) This will give a lower fraction of penetration for the surface crevasse. However, the lower rigidity of firn would tend to reduce this effect by making the extra penetrated length a lower fraction of the total rigidity of the ice column. Lai et al. (2020) show this in their supplement. More importantly, however, basal crevasses make up most of the total crevasse penetration (see Table 4 in the main text).

180 **S9: Inversion Cost Function**

175

185

We used inversions minimizing the cost function made from velocity misfit, log velocity misfit, and rigidity smoothness terms,

$$\mathcal{J} = \int_{S} w_{1} \frac{1}{2} \left(\left(v_{x} - v_{x}^{\text{obs}} \right)^{2} + \left(v_{y} - v_{y}^{\text{obs}} \right)^{2} \right) dS + \int_{S} w_{2} \left(\log \left(\frac{\|v\| + \varepsilon}{\|v^{\text{obs}}\| + \varepsilon} \right) \right)^{2} dS + \int_{b} w_{3} \frac{1}{2} \|\nabla \mathbf{B}\|^{2} db$$
 (S5)

where w_1 , w_2 , and w_3 are user assigned weights; v_x and v_y are modeled surface velocity terms; v_x^{obs} and v_y^{obs} are observed surface velocity terms; ε is a small minimum velocity for avoiding zero in the denominator; and B is the rigidity field (Larour et al., 2012). Only the first term was used except where a solution with lower velocity misfit could be found by adding the second two terms with small weights.

190 References

- Comiso, J. C.: Variability and Trends in Antarctic Surface Temperatures from In Situ and Satellite Infrared Measurements, Journal of Climate, 13, 1674–1696, https://doi.org/10.1175/1520-0442(2000)013<1674:VATIAS>2.0.CO;2, 2000.
- Cuffey, K. M. and Patterson, W. S. B.: The Physics of Glaciers, 4th ed., Elsevier, Burlington, MA, 2010.
- Fürst, J. J., Durand, G., Gillet-Chaulet, F., Tavard, L., Rankl, M., Braun, M., and Gagliardini, O.: The safety band of Antarctic ice shelves, Nature Clim Change, 6, 479–482, https://doi.org/10.1038/nclimate2912, 2016.
 - Gardner, A. S., Moholdt, G., Scambos, T., Fahnstock, M., Ligtenberg, S., van den Broeke, M., and Nilsson, J.: Increased West Antarctic and unchanged East Antarctic ice discharge over the last 7 years, The Cryosphere, 12, 521–547, https://doi.org/10.5194/tc-12-521-2018, 2018.
- Gardner, A. S., Fahnestock, M. A., and Scambos, T. A.: ITS_LIVE Regional Glacier and Ice Sheet Surface Velocities (Version 1), Data archived at National Snow and Ice Data Center [dataset], https://doi:10.5067/6II6VW8LLWJ7, 2019.
 - Getraer, B. and Morlighem, M.: Increasing the Glen-Nye Power-Law Exponent Accelerates Ice-Loss Projections for the Amundsen Sea Embayment, West Antarctica, Geophysical Research Letters, 52, e2024GL112516, https://doi.org/10.1029/2024GL112516, 2025.
- Goldsby, D. L. and Kohlstedt, D. L.: Superplastic deformation of ice: Experimental observations, Journal of Geophysical Research: Solid Earth, 106, 11017–11030, https://doi.org/10.1029/2000JB900336, 2001.
 - Howat, I. M., Porter, C., Smith, B. E., Noh, M.-J., and Morin, P.: The Reference Elevation Model of Antarctica, The Cryosphere, 13, 665–674, https://doi.org/10.5194/tc-13-665-2019, 2019.
 - Humbert, A.: The temperature regime of Fimbulisen, Antarctica, Annals of Glaciology, 51, 56–64, https://doi.org/10.3189/172756410791392673, 2010.
- Lai, C.-Y., Kingslake, J., Wearing, M. G., Chen, P.-H. C., Gentine, P., Li, H., Spergel, J. J., and van Wessem, J. M.: Vulnerability of Antarctica's ice shelves to meltwater-driven fracture, Nature, 584, 574-+, https://doi.org/10.1038/s41586-020-2627-8, 2020.
- Larour, E., Seroussi, H., Morlighem, M., and Rignot, E.: Continental scale, high order, high spatial resolution, ice sheet modeling using the Ice Sheet System Model (ISSM), Journal of Geophysical Research: Earth Surface, 117, https://doi.org/10.1029/2011JF002140, 2012.
 - Millstein, J. D., Minchew, B. M., and Pegler, S. S.: Ice viscosity is more sensitive to stress than commonly assumed, Commun Earth Environ, 3, 1–7, https://doi.org/10.1038/s43247-022-00385-x, 2022.
 - Rignot, E., Scheuchkl, B., Mouginot, J., and Jeong, S.: MEaSUREs Multi-year Reference Velocity Maps of the Antarctic Ice Sheet, Version 1, https://doi.org/10.5067/FB851ZIZYX5O, 2022.
- Roger Buck, W.: The role of fresh water in driving ice shelf crevassing, rifting and calving, Earth and Planetary Science Letters, 624, 118444, https://doi.org/10.1016/j.epsl.2023.118444, 2023.
 - Wang, Y., Zhao, C., Gladstone, R., Galton-Fenzi, B., and Warner, R.: Thermal structure of the Amery Ice Shelf from borehole observations and simulations, The Cryosphere, 16, 1221–1245, https://doi.org/10.5194/tc-16-1221-2022, 2022.